Nuclear Instruments and Methods in Physics Research A 1065 (2024) 169526

Contents lists available at ScienceDirect

Nuclear Inst. and Methods in Physics Research, A

journal homepage: www.elsevier.com/locate/nima

Full Length Article

First test beam measurement of the 4D resolution of an RSD pixel matrix connected to a FAST2 ASIC

L. Menzio [a], F. Siviero [a], R. Arcidiacono [a,b], N. Cartiglia [a,*], M. Costa [a,c], T. Croci [a], M. Ferrero [a], C. Hanna [a], L. Lanteri [c], S. Mazza [d], R. Mulargia [a,c], H-F.W. Sadrozinski [d], A. Seiden [d], V. Sola [a,c], R. White [a,c], M. Wilder [d]

[a] INFN, Torino, Italy
[b] Università del Piemonte Orientale, Italy
[c] Università di Torino, Torino, Italy
[d] University of California at Santa Cruz, CA, United States of America

ARTICLE INFO

Keywords:
FAST2
Silicon
Fast detector
Low gain
Charge multiplication
LGAD
4D tracking

ABSTRACT

This paper presents the measurement of the spatial and temporal resolutions of a Resistive Silicon Detector (RSD) pixel matrix read out by the FAST2 ASIC, a 16-channel fully custom amplifier developed by INFN Torino using a 110 nm CMOS technology. The test was performed at the DESY test beam facility with a 5 GeV/c electron beam. The RSD matrix is composed of seven 450 μm pitch pixels with cross-shaped electrodes for a total area of about 1.5 mm^2. The position resolution reached is $\sigma_x = 14 \pm 1$ μm, approximately 3.5% of the pitch, and the temporal resolution is $\sigma_t = 49 \pm 6$ ps. The work demonstrates that RSD sensors with cross-shaped electrodes achieve 100% fill factor and homogeneous resolutions over the whole matrix surface, making them a suitable choice for 4D tracking applications.

1. Introduction

Silicon sensors based on resistive readout [1], an evolution of the low gain avalanche diode (LGAD) design, combine many of the features needed by future high-energy physics experiments: (i) excellent spatial and temporal resolutions, (ii) low material budget (the active part can be a few tens of μm thick), (iii) 100% fill factor, and (iv) good radiation resistance (presently, up to $1\text{-}2 \cdot 10^{15}$ n_{eq}/cm^2). In addition, given the large pixel size, RSDs are an enabling technology for constructing 4D silicon telescopes [2] with limited power consumption as they reduce the number of readout amplifiers by more than an order of magnitude. The benefits of resistive readout are maximized when the electrode metal is minimized and shaped to limit the spread of the signal, as reported in a study using a high-precision Transient Current Technique (TCT) setup [3] to mimic the passage of particles in the sensor. The paper is structured as follows: after a brief introduction to RSD in Section 2, the test facility is explained in Section 3, and the experimental setup in Section 4. Section 5 lists notable quantities used in the analysis, and Section 6 explains the data selection, telescope, and RSD efficiency. Section 7 presents the reconstruction methods, and Section 8 the calibration and alignment procedure. Results are shown in Section 9.

2. RSD principles of operation

A short description of the RSD principle of operation is provided in this paragraph; a complete explanation can be found in [3–5]. RSDs are thin silicon sensors that combine built-in signal sharing and internal gain. A sketch of the detector cross-cut is shown in Fig. 1.

In RSD, the signal is formed on the n^+ at the hit point, and then it propagates to the electrodes. Signal formation takes about one ns, identical to that of a standard LGAD, and the propagation velocity on the n^+ is in the range 0.1–1 μm/ps, depending on the detector layout, n^+ doping level, and the value of the coupling capacitance. The signal, therefore, lasts about 1–2 ns. Since the detector is AC-coupled, an additional slow component discharges the coupling capacitors. The time constant of this discharge is also a function of the detector parameters; a full return to the baseline takes about ten ns. The sensor rate capability is, therefore, determined by the signal return to the baseline and not by signal formation.

The signal splits among the readout electrodes as a current in an impedance divider, where the impedance is that of the paths connecting the impact point to each electrode, as sketched in Fig. 2 assuming a 4-way split. The input impedance of the front-end electronics must be

* Corresponding author.
E-mail addresses: luca.menzio@to.infn.it (L. Menzio), cartiglia@to.infn.it (N. Cartiglia).

https://doi.org/10.1016/j.nima.2024.169526
Received 1 March 2024; Received in revised form 6 June 2024; Accepted 8 June 2024
Available online 10 June 2024

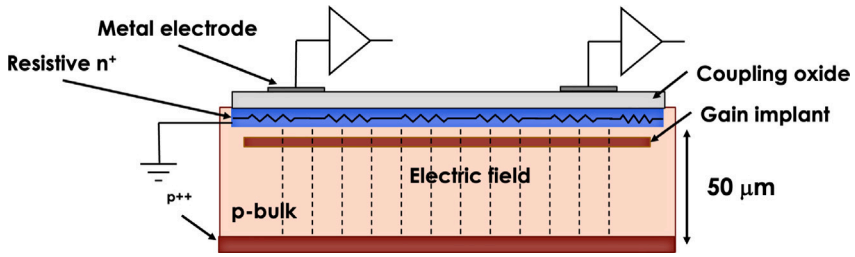

Fig. 1. Cross-cut of an RSD sensor, the key elements are indicated: a thin p-doped bulk, a gain implant, the resistive n^+ anode, the coupling oxide, and the metal electrodes.

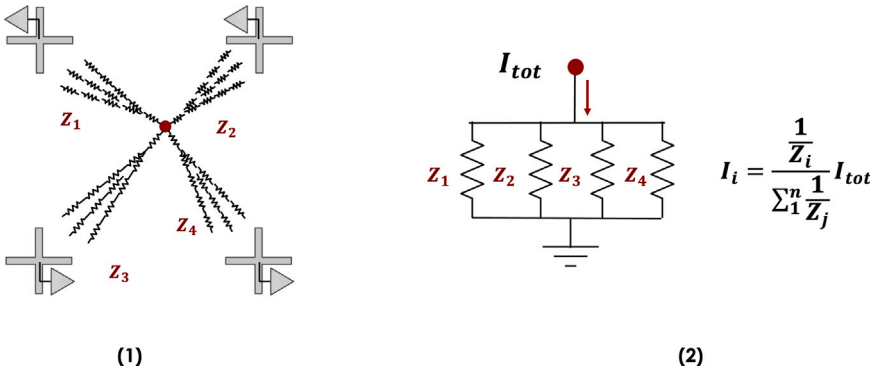

Fig. 2. Left: the signal splits among the readout electrodes. Right: the split can be computed using the equivalent circuit of a current divider.

considerably lower than the path impedances ($Z_{1,2,3,4}$) so that the signal split is governed by $Z_{1,2,3,4}$. Typical values of path impedance are in the range 1–3 kΩ.

3. The DESY test beam facility

The test beam facility in the DESY site at Hamburg–Bahrenfeld comprises three distinct beam lines providing electrons or positrons with momenta selectable in the range from 1 up to 6 GeV [6].

The test beam campaign reported in this paper was performed in the T24 experimental area. This area is instrumented with an EUDET-type telescope [7] with six planes of 54 μm-thick MIMOSA-26 Monolithic Active Pixel Sensors [8], three planes upstream of the DUT and three downstream. An AIDA-2020 Trigger Logic Unit [9] provided the trigger to the telescopes. The data acquisition was performed in the EUDAQ2 framework [10]. The telescope performance depends on the six planes' relative positions, the beam energy, and the DUT material budget. A resolution of $\sigma_x = 1.83 \pm 0.03$ μm is predicted [7] using a distance of 20 mm between the telescope planes, a 20 mm distance between the DUT and the closest telescope planes, a ∼ 100 μm thick silicon DUT, and a beam momentum of 5.0 GeV/c. The resolution degrades with increasing DUT thickness and distance between the DUT and the closest telescope planes: for a ∼ 500 μm thick silicon DUT, and a distance DUT-telescope of 100 mm is about $\sigma_x = 6.5$ μm.

4. The experimental setup

In this paragraph, the key elements of the experimental setup are presented. The system comprises the FAST2 ASIC, an RSD2 sensor, a readout board, and the data acquisition system.

4.1. The FAST2 ASIC

The FAST2 ASIC [11,12] is designed using standard 110 nm CMOS technology; its power consumption is 2.4 mW/ch. It has a footprint of about 5 × 1.5 mm^2. FAST2 has been designed in two versions: (i) an amplifier-comparator version (FAST2D) with 20 readout channels and (ii) an amplifier-only version (FAST2 A) with 16 channels. The FAST2 front-end circuit comes in two versions, EVO1 and EVO2. Both versions use the same input stage design, a transimpedance amplifier with two amplification stages but use different technical implementations: EVO1 uses standard transistors, while EVO2 uses RF transistors. Overall, the two designs have similar performance; EVO1 is preferred since it has a slightly lower noise and a larger dynamic range. The first eight channels of FAST2 A are of the EVO1 type, while the other 8 are of the EVO2 type. Laboratory tests with a beta telescope have shown that the FAST2 A, when coupled with an LGAD pixel with a capacitance of ∼ 3 pF, reaches a resolution of about 50 ps for an LGAD gain above 20. FAST2 A has two programmable features: (i) an internal test-pulse generator used for calibration and (ii) the preamplifier gain. Depending on the gain selection, the bandwidth varies between 230 and 665 MHz and the peaking time between 0.49 and 1.2 ns. If not programmed, the FAST2 ASIC signal amplitude is ∼ 10 mV/fC or, equivalently, has a transimpedance of ∼ 6 kΩ with a bandwidth of 580 MHz, and an input impedance of 165 Ω. In this work, FAST2 A has been used.

4.2. The RSD2 sensor

The sensor used in this test belongs to the FBK RSD2 production [13]. RSD2 comprises 15 p-type 6" wafers, including epitaxial and float-zone (Si-Si) types. The active volume is either 45 or 55 μm thick, attached to a 450 μm handle wafer. The wafers differ in the doping level of the gain implant and the resistivity of the n^+ implant. The sensor used in this test is from wafer 4; it has a float-zone 55 μm-thick active volume. Fig. 3 shows the gain versus bias curve of the sensor measured at the test beam. The red dots indicate the voltages used in this paper. The curve is obtained by converting the FAST2 A signal amplitude into charge using the conversion constant 10 ± 1 mV/fC. This factor was measured in the laboratory, combining results obtained using the FAST2 internal calibration capability, laser runs taken with a TCT, and MIP data collected with a beta source.

The sensor used in the test is a 6 × 6 matrix of electrodes with a 450 μm pitch. The electrodes are cross shaped, with arms extending in the x and y directions, leaving a small gap between two adjacent arms. The gap length varies from 10 to 40 μm, while the width of the arm is fixed at 20 μm. During the test, 14 electrodes were read out, for a total

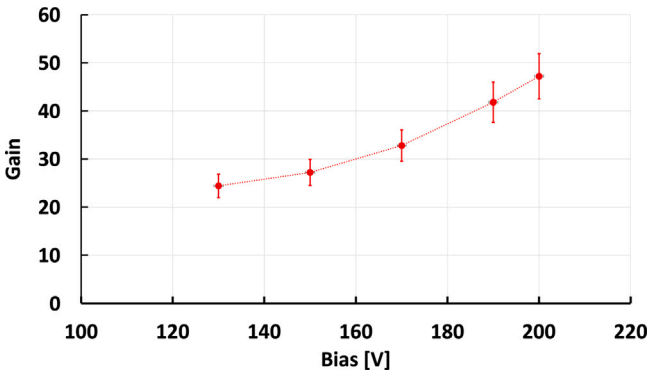

Fig. 3. The DUT gain versus bias characteristics.

of 7 pixels; 8 electrodes were connected to the EVO1 channels of FAST2 and the remaining 6 electrodes to FAST2 EVO2. The other electrodes were grounded. Fig. 4 shows on the left side a picture of the sensor and on the right side the schematic of the electrodes.

4.3. The FAST2-RSD readout board

The RSD2 sensor and the FAST2 ASIC were mounted on a custom Printed Circuit Board (PCB), about 1 mm thick. The ASIC section of the board is powered by a single voltage line at 4.0 V, and via voltage regulators provides the power to the ASIC. The sensor section of the board provides the sensor bias voltage via a low-pass filter. The board houses 16 MCX connectors for the FAST2 output signals. Fig. 5 shows a picture of the board used in this test. The connections from the sensor to the ASIC were made with two sets of wire bonds, using intermediate pads to ensure the possibility of changing the sensor without damaging the ASIC. The board can be instrumented with an Arduino microcontroller to program the FAST2 settings. The controller was not mounted for this test, so FAST2 worked at the default gain setting.

4.4. The acquisition system

A schematic of the data acquisition system used during the test beam is shown in Fig. 6. The setup has a trigger path (left side of the figure) and a data path (right side of the figure):

- Trigger path: the initial trigger is generated by an electron hitting the Photonis MCP-PMT (model FT-8 Hi QE UV) [14]. The MCP triggers, in high impedance, (line 1) the LeCroy HD040 oscilloscope [15] that, in turn, triggers (line 2) a CAEN logic unit [16], used to duplicate the oscilloscope trigger. The logic unit triggers (line 3) the AIDA-2020 TLU [17] and the CAEN DT 5742 Digitizer [18] (~ 500 MHZ analog bandwidth, 5 GS/s) used to read out the DUT. Finally, the TLU triggers (line 4) the EUDET telescope data acquisition (EUDAQ2).
- Data path: upon trigger arrival, the signals from the MCP and the DUT are digitized by the CAEN Digitizer and stored on the DAQ PC, while the data from the telescope are saved on the EUDAQ2 PC together with the trigger stamp from the TLU. The digitizer provides 6–7 samples on the signal rising edge.

The bias voltage to the sensor and the MPC were provided by a CAEN DT 1471ET [19] unit. The DUT and beam telescope's data acquisition systems run independently, each producing a file per run, merged offline. The merging operation checks for the possibility that a spurious trigger on either system misaligns the streams of events and, when this happens, realigns the two files. The realignment is based on the requirement that a track pointing to one of the RSD active electrodes generates an RSD signal above A^{min} (defined in Section 5).

5. Notable quantities used in the analysis

Table 1 reports definitions and variables used in this study, the lower index refers to the component (trigger, electrode i, pixel) while the upper index specifies what is measured. The numerical values of some of these parameters, determined during the analysis, are reported here for reference.

6. Signal properties, data selection, and telescope and RSD efficiency

Fig. 7 shows on the left an example of the FAST2 output signals recorded at the test beam with 5 GeV/c electrons. As expected, the signal is bipolar due to the sensor AC coupling, the signal has a triangular shape determined by the convolution of the RSD output current with the FAST2 A and digitizer shaping times (the combined bandwidth is ~ 450 MHz); it has a rise time of ~ 1 ns and a slightly longer fall time. On the right side of Fig. 7, the distribution of the baseline value at −5 ns with respect to the signal peak is reported for all events taken in the run at bias = 190 V. The amplitude RMS, ~ 1 mV, shows that the electronic noise is rather small, yielding a signal-to-noise ratio above 50 for signals above 5 fC (sensor gain of 10 assuming the signal collected in a single electrode). The amplitude RMS of the sum of two baseline samples separated by 1 ns is 1.43 mV, slightly higher than what it would be for fully uncorrelated noise, $0.954 \times \sqrt{2} = 1.35$ mV.

Fig. 8 illustrates a few important properties of the events recorded by the DUT:

1. The signal amplitude on a given electrode (el = 5 in the plot) is visible for a distance of about $\sqrt{2}$ × pitch ~ 675 μm, i.e. one pixel.
2. The signal rise time remains constant for about the arm length, 200 μm, and then increases with distance.
3. The mean value of A_{pixel} is constant at the center of the pixel, increasing by ~ 10% at the edge (here, the projection on the x axis is shown).
4. A_{pixel} follows a Landau distribution as a standard LGAD

6.1. Data selection

The MCP triggered the events recorded at the test beam. Tracks reconstruction was performed using the Corrivreckan package [20] and the General Broken Lines algorithm has been used to account for the multiple scattering effects of 5 GeV/c electrons on the telescope and DUT materials. The pixel noise threshold was set to the default threshold4 setting. Noisy pixels in the telescope were masked, and events with multiple tracks were discarded. The tracks were selected requiring six hits (one per plane) and $\chi^2/ndof < 10$. The percentage of MCP triggers with a reconstructed track is about 64%. Fig. 9 (a) shows A^{max} for tracks pointing more than 500 μm away from the RSD sensor: as expected, most of the events have a low A^{max}; however, about 0.7% of the events have a large RSD signal. The A^{max} distribution of these events is consistent with good RSD events, indicating a problem with the track reconstruction. Fig. 9 (b) reports the A^{max} quantity for the events with an RSD track. In this plot, two families of events are visible: the majority of events have a large RSD signal; however, a small fraction, about 3%, has an RSD signal consistent with noise events, $A^{max} < A^{min}$. The events in the noise peak are due to either poor track reconstruction or RSD inefficiency. Fig. 9(c) (d) shows the distribution of the telescope x_{trk} (y_{trk}) coordinate for good events (black line) and for the events in the noise peak of (b). The two plots indicate that the events in the noise peak are uniformly distributed over the area of the seven active pixels and do not cluster in a specific RSD location. Given the difficulties in separating the RSD efficiency from the telescope efficiency, only a lower RSD efficiency limit, about 97%, can be set.

Good events are defined as those passing the following four requirements:

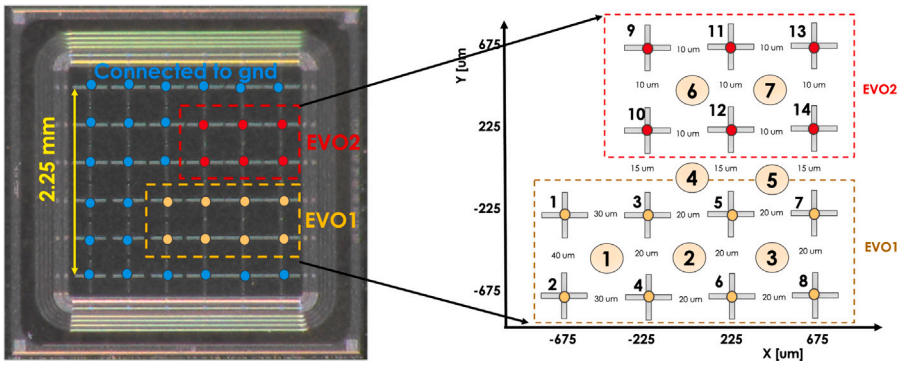

Fig. 4. Left: a picture of the sensor used in this test, with the electrodes in blue connected to ground, in yellow to EVO1, and in red to EVO2. Right: a schematic of the electrodes, the pixels, the gap between the metal arms, and the x-y reference system used in the analysis.

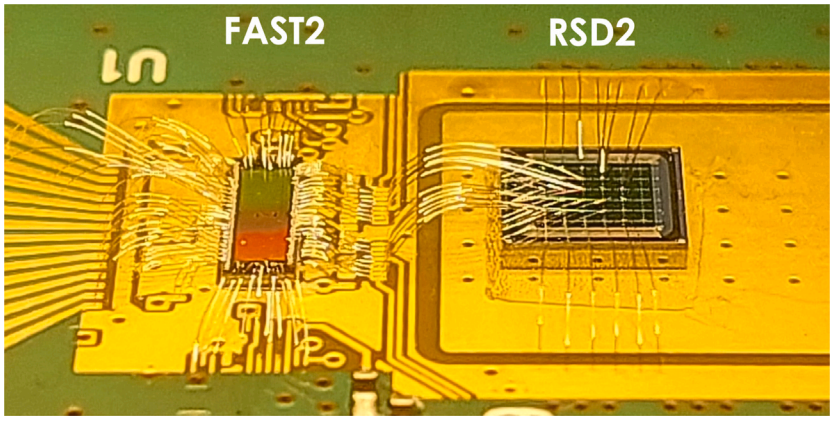

Fig. 5. Image of the RSD2 sensor wire-bonded to the FAST2 ASIC on the readout board.

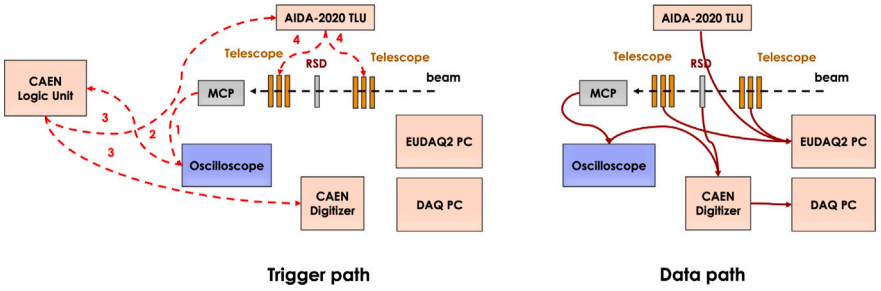

Fig. 6. Schematic of the data acquisition system. Left: the trigger path. Right: the data path.

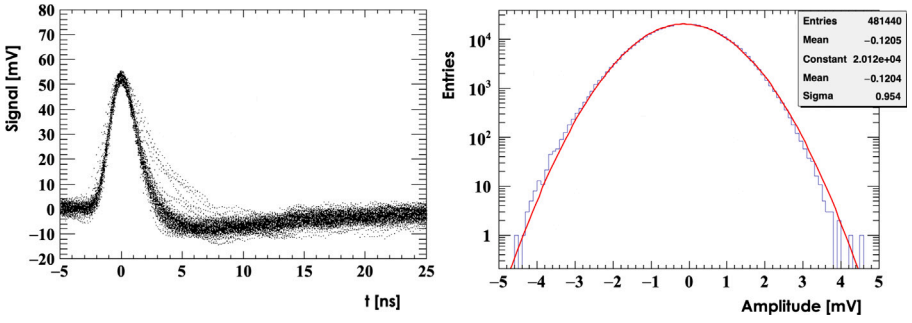

Fig. 7. Left: FAST2 A EVO1 output signals. The events in the picture were selected by requiring an amplitude of 50–54 mV. Right: distribution of the baseline value at −5 ns with respect to the signal peak. The overlapped Gaussian fit shows the almost complete absence of non-Gaussian tails. Both plots use events taken at a bias = 190 V.

Table 1
Definitions and variables used in this study. When a variable is computed at a given signal fraction, for example CFD30, the value is obtained with a linear interpolation of the sample positions right above and right below the requested point.

Definitions	
Good events	Events passing the selection presented in Section 6.1
Active electrodes	The 14 electrodes read out during the test.
Active pixels	The 7 pixels read out during the test.
Good track	A track with one hit in each of the 6 telescope planes and $\chi^2/ndof < 10$.
RSD track	A good track pointing to an active pixel, i.e., the track x-, y- coordinates at the DUT within 225 μm to any of the nominal pixel centers.
Event variables	
A_i, A_{MCP}	The signal amplitude of electrode i or the MCP. The signal amplitude is defined as the peak of the parabola fitted to the 6 highest samples.
A^{max}	The highest amplitude among the 14 electrodes.
A_{all}	The sum of the 14 signal amplitudes. This sum is computed when A^{max} is on either electrode 5 or 12 to ensure full signal containment among the active electrodes.
A_{pixel}	The amplitude measured by a pixel, defined as the sum of the amplitudes seen by the electrodes at the 4 corners of the pixel.
A^{max}_{pixel}	The highest pixel amplitude.
A_i^{CFD30}	The 30% amplitude of A_i (CFD: Constant Fraction Discriminator).
t_i^{meas}	The electrode i hit time measured at A^{CFD30} .
t_i^{rise}	The 20%–80% signal rise time of electrode i.
$t_{trigger}$	The MCP hit time, measured at A_{MCP}^{CFD30}.
Global variables	
$\sigma_i^{sample} = 0.95$ mV	The standard deviation of a point on the baseline, measured in the absence of signal.
$\sigma_i^{amplitude} = 2.3$ mV	The standard deviation of the amplitude. It depends on noise σ_i^{sample} and the fitting procedure.
$\sigma_i^{CFD30} = 2.5$ mV	The standard deviation of A_i^{CFD30}. It depends on σ_i^{sample} and the fitting procedure.
$\sigma_{trigger} = 38 \pm 8$ ps	The resolution of $t_{trigger}$, evaluated in the laboratory.
$\sigma_{telescope} = 8 \pm 1.5$ μm	The resolution of the DESY telescope, calculated using the GBL calculator.
$A^{min} = 15$ mV	The minimum amplitude among the 14 electrodes to identify an RSD signal.
MPV_{all}, MPV^{max}_{pixel}, MPV_i	The most probable value of the Landau fit to the A_{all}, A^{max}_{pixel}, A_i distributions.

Table 2
List of runs used in this work.

Bias [V]	Good tracks [k]	Good events [k]	MPV_{all} [mV]	MPV^{max}_{pixel} [mV]	Gain	Saturated events %	RSD track $A^{max} < A^{min}$ %
130	277	5.2	122	77	24	3.0	4.0
150	285	6.8	136	93	28	3.8	2.9
170	309	7.5	164	118	33	6.2	3.0
190	175	4.3	209	157	42	11	3.0
200	284	6.5	236	175	47	18.9	2.8

- An RSD track
- $A^{max} > A^{min}$,
- t_i^{hit} of the highest signal within 1 ns of $t_{trigger}$,
- $A^{max} < 250$ mV for EVO1 electrodes and $A^{max} < 220$ mV for EVO2 electrodes.

Table 2 lists the properties of the runs used in this work. The second to last column lists the % of FAST2 saturated events, while the last column lists the % of RSD tracks without an RSD signal.

7. The reconstruction methods

7.1. Reconstruction of the hit position

The determination of the hit position in a RSD is achieved by combining the information from 4 electrodes. In this study, the hit position was reconstructed using two different algorithms: (i) the Discretized Position Circuit (DPC) [21], and (ii) the Sharing Template (ST).

7.1.1. The discretized position circuit (DPC) reconstruction method

In DPC, the position is reconstructed using the signal amplitude imbalance between the two sides (right–left, top–bottom) of the pixel. Using as an example pixel 1 of Fig. 4, the DPC equations are:

$$x^{meas} = x_0 + \frac{pitch}{2} * \frac{(A_3 + A_4) - (A_1 + A_2)}{\Sigma_1^4 A_i}$$
$$y^{meas} = y_0 + \frac{pitch}{2} * \frac{(A_1 + A_3) - (A_2 + A_4)}{\Sigma_1^4 A_i}, \quad (1)$$

where x_0 and y_0 are the coordinates of the central point of the pixel.

As explained in [3], the x, y coordinates calculated with Eq. (1) suffer from systematic shifts that can be compensated by using a

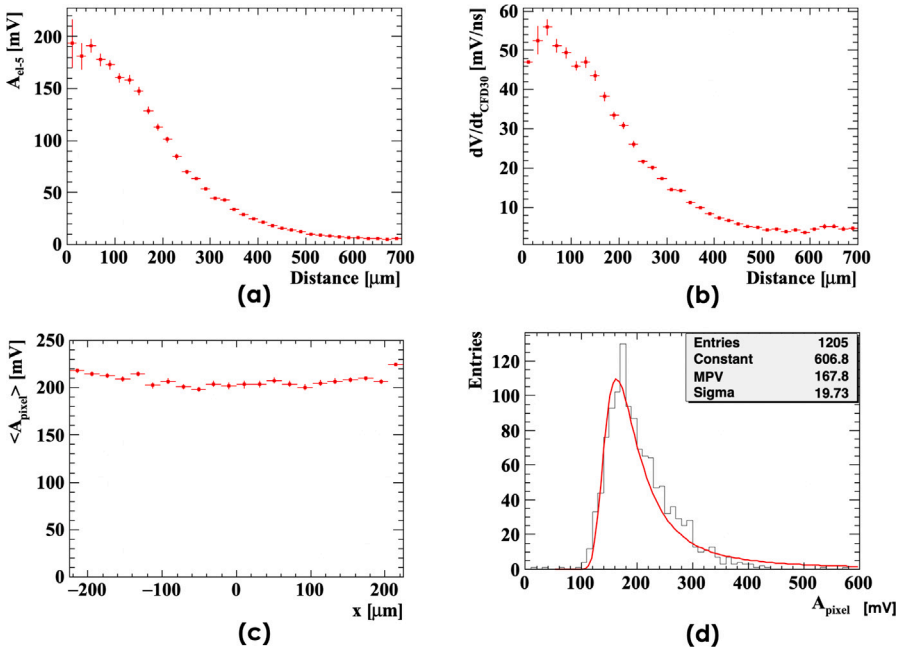

Fig. 8. (a) Signal amplitude as a function of the hit distance from the electrode. (b) Signal slew rate at the CFD30 point as a function of distance. (c) Projection on the x-axis of A_{pixel} over the pixel area. (d) A_{pixel} distribution of the good events hitting pixel 2. Events taken at bias = 190 V.

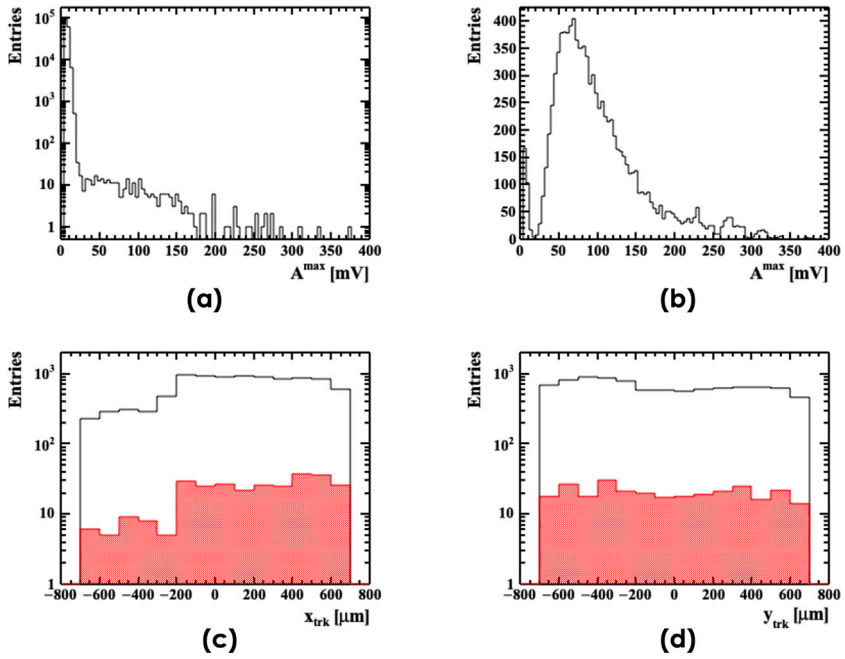

Fig. 9. (a): A^{max} distribution for tracks pointing outside the RSD sensor. (b) A^{max} distribution for the events with an RSD track. (c), (d): spatial distribution of the telescope x, y coordinate for all good events (solid line) and for events without an RSD signal above A^{min} (red histogram). The plots have been taken with bias = 170 V.

migration map. In this analysis, the migration map was computed at the TCT laser setup in the Torino laboratory employing a sensor with the same layout but different n^+ resistivity, read out by a 16-channel amplifier board developed at the FNAL [22].

A given migration map corrects the shifts introduced by the reconstruction method and all other effects that cause uneven signal sharing. These additional corrections, for example, due to inhomogeneities of the sensor's n+ resistive layer or differences in the electronics input impedance, are specific to the hardware used to compute the migration map. When these additional terms are sub-leading [3], a migration map can be used for all sensors with the same geometry.

7.1.2. The sharing template (ST) reconstruction method

The second position reconstruction method, ST, uses a template of the signal sharing among the 4 electrodes as a function of the hit position in the pixel. For each position, the fraction of signal in the 4 electrodes is tabulated in a template. For every event, the fraction of signal in each electrode is computed and compared with the prediction

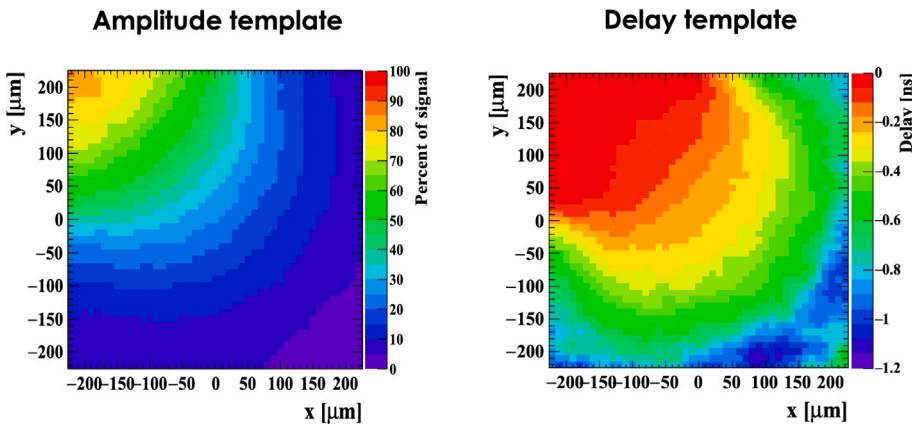

Fig. 10. Templates for the top left electrode of a pixel: Left: percentage of the signal as a function of position. Right: signal delay as a function of position.

of the template. The left plot of Fig. 10 shows the percentage of the signal seen by the top left electrode of a pixel, as computed using data collected at the DESY test beam. In this study, the template is computed in a grid of 10×10 µm^2 cells, and, to increase statistics, the events from all 7 active pixels are summed. The events for the analysis and those used to build the templates belong to different data sets.

The hit position determination using the ST method is as follows:

- For each cell k of the template, the sum of the amplitude-weighted differences between the measured ($f_i^{measured}(k)$) and tabulated ($f_i^{tabulated}(k)$) signal fractions of the 4 electrodes is computed: $\chi^2(k) = \Sigma_{i=1}^{4}((f_i^{measured}(k) - f_i^{tabulated}(k)) * A_i)^2$, where i is the electrode index.
- The coordinates of the cell k with the minimum $\chi^2(k)$ provide the seed position.
- The hit position is computed as the χ^2 weighted centroid of the 3×3 cells centered at the seed cell.

The spatial resolution can be expressed as:

$$(\sigma^{hit\ pos})^2 \approx (\sigma^{pos-jitter})^2 + (\sigma^{reconstruction})^2 + (\sigma^{setup})^2 + (\sigma^{sensor})^2. \quad (2)$$

- $\sigma^{pos-jitter}$: for a single electrode i, this term depends linearly on the uncertainty of the amplitude determination $\sigma_i^{amplitude}$ and the signal variation per unit length dA_i/dx:

$$\sigma_i^{pos-jitter} = \sigma_i^{amplitude}/(dA_i/dx). \quad (3)$$

  Combining 4 electrodes and assuming equal noise and amplitude variation with distance for all electrodes, the above expression leads to:

$$\sigma^{pos-jitter} \propto \frac{\sigma^{amplitude}}{\Sigma_i A_i} \times pitch. \quad (4)$$

- $\sigma^{reconstruction}$: term that depends on the position reconstruction method
- σ^{setup}: due to hardware-related effects such as differences in gain among amplifiers or misalignment between the device under test and the reference tracking system.
- σ^{sensor}: term grouping all sensor imperfections contributing to an uneven signal sharing among electrodes, for example, a non-uniform n^+ implant.

The jitter term decreases with the sum of the signal amplitudes, while the other three terms contribute to the constant term, the systematic limit of the measurement.

7.2. Reconstruction of the hit time

In contrast with the hit position reconstruction, where the information from multiple electrodes is needed, the hit time reconstruction

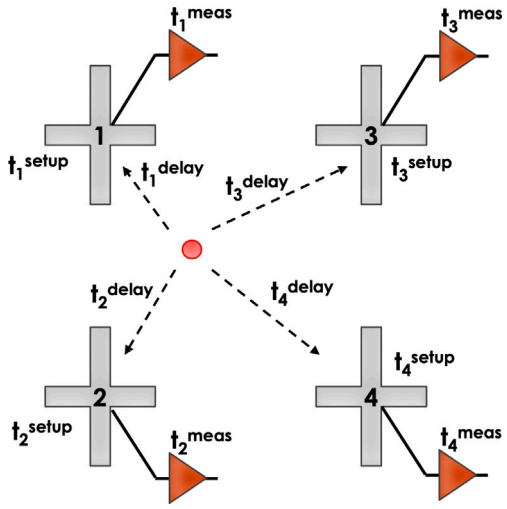

Fig. 11. Schematic of the various contributions to t_i^{hit}.

is performed separately by each electrode. For each electrode, i, the measured time, t_i^{meas}, differs from the hit time due to the delay, t_i^{delay}, introduced by the signal propagation on the resistive layer. Therefore, the reconstructed hit time t_i^{hit} can be expressed as:

$$t_i^{hit} = t_i^{meas} + t_i^{delay}(x, y) + t_i^{setup} \quad (5)$$

where t_i^{setup} is a hardware-specific offset due to PCB traces and cable lengths. The delay as a function of position has been tabulated in a template computed using test beam data, shown in the right plot of Fig. 10. Given the cross-shaped electrodes, the delay does not increase linearly with distance but has a broad region near the electrode where the signal has a minimum delay. Fig. 11 illustrates the various contributions to t_i^{hit}.

The temporal resolution associated with t_i^{hit} is the sum of 3 terms:

$$(\sigma_i^{hit\ time})^2 = (\sigma_i^{time-jitter})^2 + (\sigma_i^{Landau\ noise})^2 + (\sigma_i^{delay})^2 \quad (6)$$

where:

- $\sigma_i^{time-jitter}$ depends linearly on the noise σ_i^{CFD30} and the signal derivative at A_i^{CFD30}:

$$\sigma_i^{time-jitter} = \sigma_i^{CFD30}/(dV/dt)|_{A^{CFD30}} \sim \frac{\sigma_i^{CFD30}}{A_i} \times t_i^{rise}, \quad (7)$$

- $\sigma_i^{Landau\ noise}$ is due to non-uniform ionization. Assuming a 50 µm thick sensor, this term is about 30 ps [23].

- σ_i^{delay} is due to the uncertainty on the hit position reconstruction, it can be minimized with a good determination of the impact point.

The uncertainties of the 4 electrodes are not independent since a part of $\sigma^{time-jitter}$ might be due to common electronic noise, $\sigma^{Landau\ noise}$ is the same for the 4 electrodes (in a given event, the same signal shape is seen by the 4 electrodes), and σ^{delay} affects all t_i^{hit}. The 4 t_i^{hit} estimators can be combined in a χ^2 function to estimate the hit time t^{hit}, however under these conditions the covariance matrix Ω is not diagonal:

$$\chi^2(t^{hit}) = \sum_{i=1}^{4}\sum_{j=1}^{4}(t^{hit} - t_i^{hit})\Omega_{i,j}^{-1}(t^{hit} - t_j^{hit})$$
$$\frac{\partial\chi^2}{\partial t^{hit}} = 0 \rightarrow t^{hit} = \frac{\sum_{i,j=1}^{4} t_i^{hit}(\Omega^{-1})_{i,j}}{\sum_{i,j=1}^{4}(\Omega^{-1})_{i,j}} \quad (8)$$

where Ω^{-1} is the inverse of the covariance matrix.

If the uncorrelated jitter term is the dominant source of uncertainty, Ω^{-1} is diagonal and t^{hit} can be expressed as:

$$t^{hit} \sim \frac{\sum_i^4 t_i^{hit} * A_i^2}{\sum_i^4 A_i^2} \quad (9)$$

where identical σ_i^{CFD30} and t_i^{rise} are used.

7.3. Determination of the telescope spatial resolution

The test beam telescope resolution has been evaluated using the General Broken Lines (GBL) track resolution calculator tool [24]. This program considers the positions of the six telescope planes, the DUT position, and the material budget of the DUT to estimate the spatial resolution of the tracks extrapolated at the DUT position. Using the first plane hit by the beam as a reference, the telescope planes were positioned at 0.0, 135.1, 213.3, 389.5, 480.1, and 563.7 mm along the beam direction, and the DUT at 281.2 mm. Taking into consideration possible plane misalignments and errors in the evaluation of the material budget, the telescope resolution has been calculated to be $\sigma_{telescope} = 8 \pm 1.5$ μm in the x and y directions. This value is consistent with the calculations shown in [7].

7.4. Determination of the trigger temporal resolution

The MCP signal is very fast, with a rise time of about 50–100 ps: this is the key to its excellent temporal resolution. In the laboratory studies carried out in Torino, the MCP is read out by a fast scope with an analog bandwidth of 4 GHz. In this configuration, the MCP resolution has been evaluated to be about 12 ± 2 ps. However, in the present study, the MCP is read out by a CAEN digitizer that, given its analog bandwidth of 500 MHz, limits the rise time of the MCP signal to 0.6–0.7 ns. The resolution of the MCP connected to a CAEN digitizer was evaluated in the laboratory by comparing the width of the distribution $t_{MCP}^{CFD30} - t_{LGAD}^{CFD30}$ of a run taken with the MCP read out by a fast oscilloscope to that of a run where the MCP was connected to the CAEN digitizer. The test was performed using a β source, a 50 μm thick LGAD from Hamamatsu biased to have a gain of about 20, and the FAST3 [25] analog ASIC. This procedure yielded an MCP resolution of 40 ± 8 ps for the combination MCP-Digitizer. The MCP signal MPV in a β run is smaller than the MPV obtained at the test beam, 8 mV versus 14 mV. To take into account this additional fact, an additional β run was taken where the MCP signal was boosted by a 20 db Cividec C1 amplifier [26] (2 GHz analog bandwidth) before being connected to the digitizer. Under this condition, the MCP MPV was about 42 mV, and the resolution was 25 ± 5 ps. Since the digitizer dominates the noise, it can be assumed that the MCP temporal resolution scales with the signal amplitude; the MCP resolution at the test beam was determined to be $\sigma_{trigger} = 38 \pm 8$ ps.

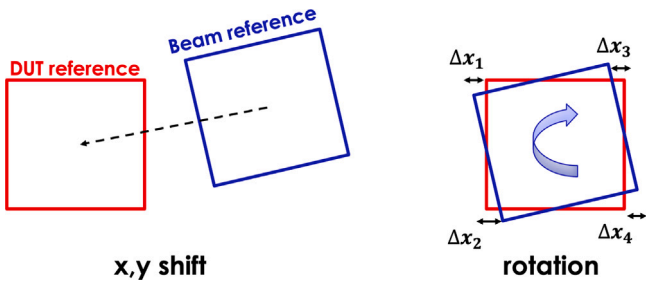

Fig. 12. Alignment procedure: first, the x-, y- offset is computed, then a rotation is applied.

8. Calibration and alignment

8.1. FAST2 calibration and saturation

To ensure uniform response across the 7 pixels, the amplifier response of the 14 FAST2 channels, 8 EVO1 and 6 EVO2, have been equalized by imposing that the MPV_i is the same for all electrodes. The calibration constants are the same for all runs and vary between 0.9 and 1.1.

The FAST2 output signal saturates at about 300 mV (∼ 30 fC) for EVO1 channels and at about 250 mV (∼ 25 fC) for EVO2 channels. The percentage of saturated events, as reported in Table 2, goes from 2% at bias = 130 V to 19% at bias = 200 V. In saturated events, the position reconstruction is altered as the signal amplitudes of the four electrodes do not correspond to the actual signal split and the reconstructed position tends to be shifted toward the center of the pixel. The temporal resolution is also degraded since saturated signals have a different shape, shifting the position of the point used for time reconstruction (CFD = 30%). Their inclusion in the analysis degrades the position and temporal resolutions by about 6% at bias = 200 V, and by less than 3% at 170 V.

8.2. DUT-telescope alignment

The telescope and the DUT have been aligned with a software procedure by introducing an x- and y-offset and a rotation. The offset and the rotation were applied to the telescope reference system.

The offset was computed by exploiting the fact that the mean value of the telescope x (y) hit positions should be centered on the nominal x (y) position of the electrode with the highest amplitude. The data were divided into 14 histograms, one per electrode, each containing the telescope hit position for the events where that specific electrode has the highest signal. The difference between the telescope mean value and the electrode coordinate, $\Delta x_i = (\langle x_{track}\rangle - x_{el-max=i})$, is the optimal shift for electrode i. Given the presence of a rotation, it is impossible to find a single shift in x (y) that minimizes the 14 Δx_i at once; what should be minimized is the sum all Δx_i.

After having determined the best shift, the rotation was computed by minimizing the sum of the absolute value of the distances. The rotation was found to be $\theta = -0.025$ radiants. This procedure is shown in Fig. 12.

9. Test beam results

9.1. Spatial resolution

For each of the bias voltages listed in Table 2, the spatial resolution in x and y were computed with two different algorithms: (i) the DPC method and (ii) the ST method. Fig. 13 shows the x-, y- resolution measurements at the bias voltage 170 V using the ST method. The plots (a) and (b) demonstrate the very good correlation between the

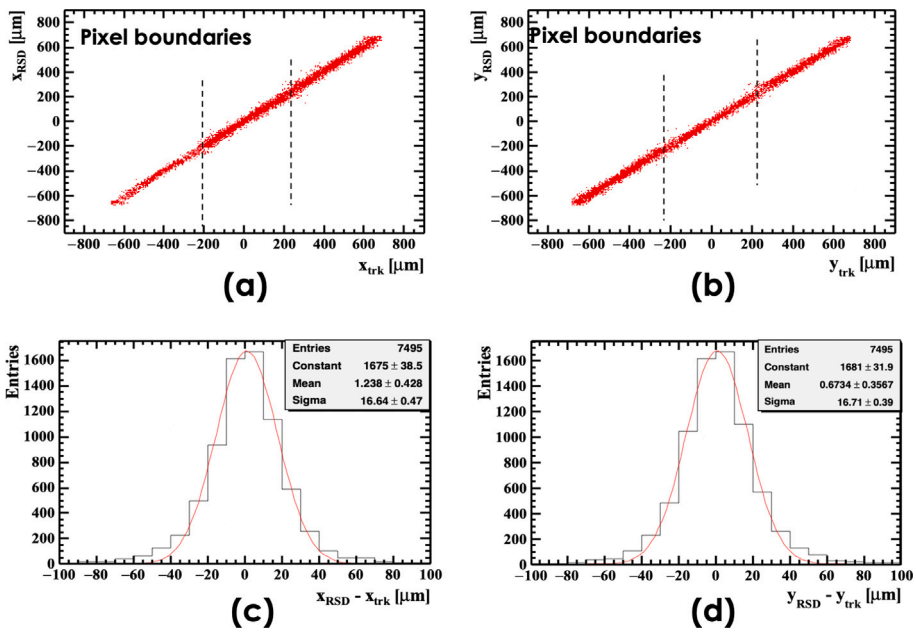

Fig. 13. (a) and (b): correlation between the telescope and RSD coordinates integrating over all active pixels. The dashed lines indicate the pixel boundary. (c) and (d): distributions of the x and y telescope and RSD coordinate differences integrating over all active pixels. All plots are obtained using the ST method. Each histogram is fitted to a Gaussian (red line). The data shown were collected at bias = 170 V.

telescope hit positions x_{trk}, y_{trk} and the RSD positions, x_{RSD} and y_{RSD}, respectively. Notably, the telescope-RSD excellent correlation continues seamlessly across pixel boundaries, demonstrating that RSDs have 100% fill factor.

Plots (c) and (d) report the distributions of the differences $(x_{RSD} - x_{trk})$ and $(y_{RSD} - y_{trk})$ fitted to a Gaussian distribution. The reported values of $\sigma_x \sim 17$ μm and $\sigma_y \sim 17$ μm are the convolution of the RSD and telescope resolutions. The non-Gaussian tails, defined as the difference between the histogram entries and the fitted distribution in the regions above and below two standard deviations from the histogram mean, account for 7.3% of the events. The origin of these tails is further discussed at the end of this Section.

Including the saturated events, the spatial resolution increases by about 0.7 μmat bias = 200 V, by 0.5 μm at bias = 190 V, and by less than 0.3 μm at bias = 170 V.

Fig. 14 reports the RSD resolution at each bias voltage for the two methods after subtracting in quadrature $\sigma_{telescope} = 8 \pm 1.5$ μm. The slightly worse results of the DPC method can be understood considering that the migration map was computed using the laboratory TCT setup with a different sensor and electronics, while the sharing template of ST was calculated with test beam data and the same hardware used in the analysis.

The resolution is below 25 μm for both methods, even at the lowest gain, and, for the ST method, reaches a constant value of $\sigma^{hit\ pos} \sim 15$ μm for a gain above 30.

The spatial resolution can be fitted as the quadrature sum of a constant and a jitter term, according to Eq. (2), given by:

$$\sigma^{hit\ pos} = \sqrt{(\sigma^{pos-constant})^2 + (\frac{\sigma^{amplitude} \times pitch}{\Sigma_i^4 A_i})^2}. \quad (10)$$

Fig. 15 shows the fit to the ST results as a function of A_{pixel}. As expected, the jitter term becomes subleading as the gain increases. Starting at gain ~ 25, the resolution is dominated by the constant term, $\sigma^{pos-constant} = 12 \pm 1$ μm.

Following the expression of Eq. (2), the constant term includes contributions from the reconstruction method, the experimental setup (for example, FAST2 response and telescope-DUT alignment), and sensor non-uniformity. Given the small jitter term, the position resolution is weakly dependent on the gain, indicating that RSD can provide excellent position resolution over a wide range of bias voltage.

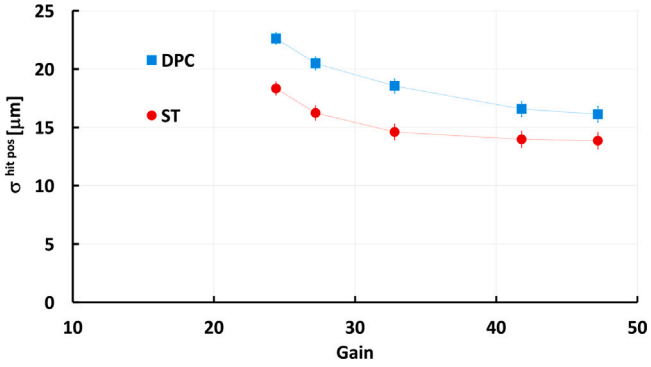

Fig. 14. RSD resolution integrated over all active pixels for the two reconstruction methods.

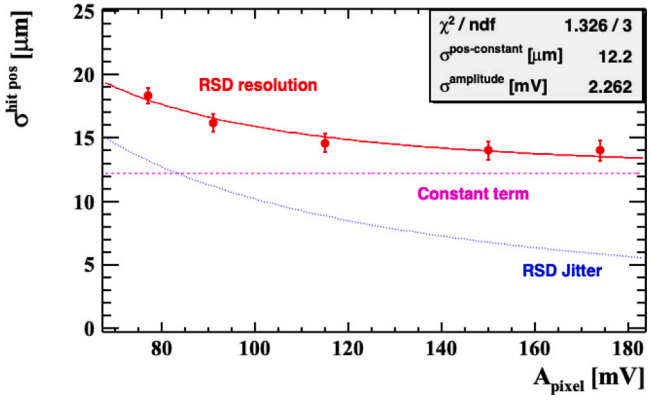

Fig. 15. RSD position resolution (ST) as a function of A_{pixel}. The resolution is fitted as the sum of a jitter and a constant term. The constant term dominates the resolution above gain ~ 25.

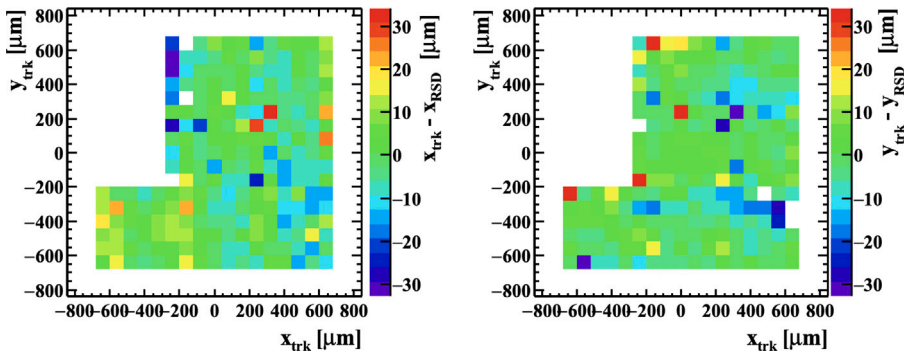

Fig. 16. Left: the difference $x_{trk} - x_{RSD}$ in the $x_{trk} - y_{trk}$ plane for the 7 pixels used at the test beam. Right: The same plot is for the y coordinate. The points below two standard deviations are shown in blue, while those above are in red. The plots are obtained using the ST method. The data shown were collected at bias = 170 V.

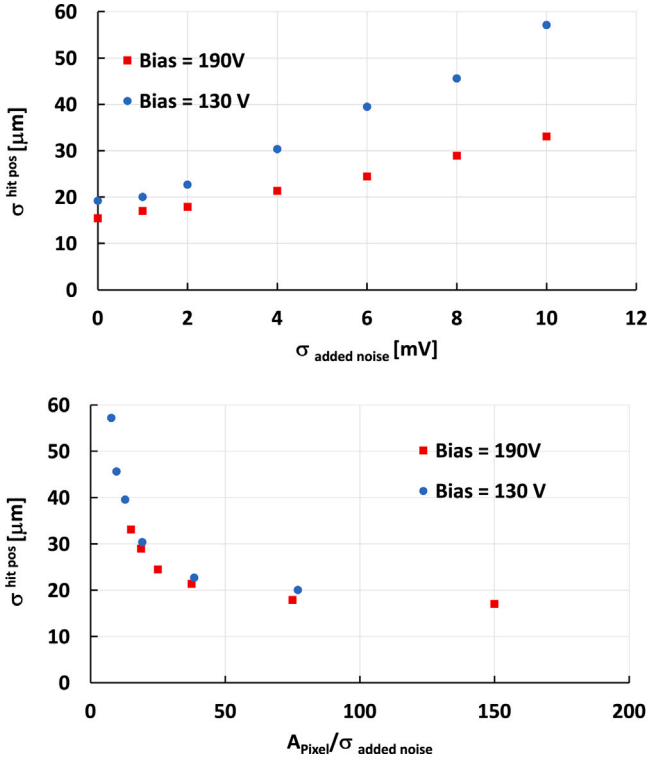

Fig. 17. Degradation of the spatial resolution as a function of added noise. Top: spatial resolution plotted versus the sigma of the added Gaussian noise. Bottom: the same data plotted versus the signal-to-added-noise ratio.

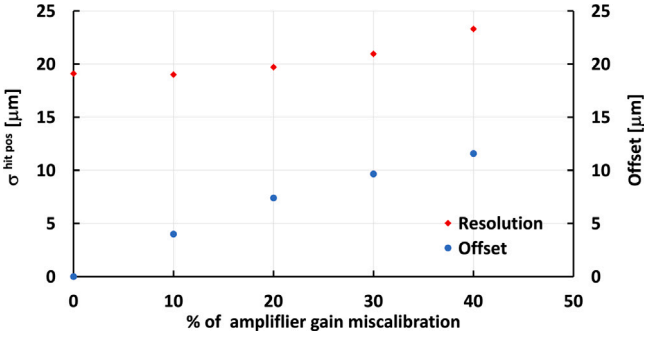

Fig. 18. Position resolution and offset as a function of the % of one amplifier gain miscalibration. The study is performed using the run with Bias = 130 V.

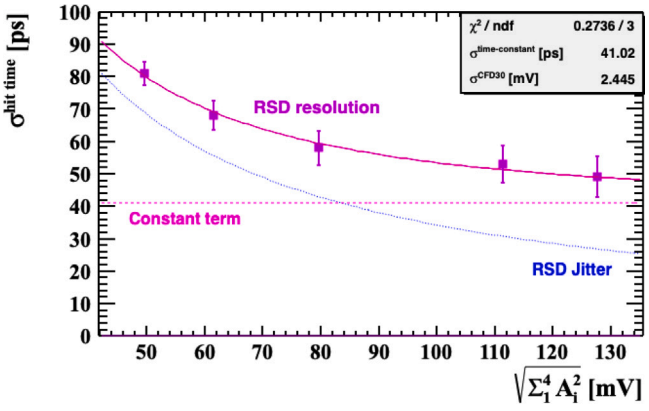

Fig. 19. RSD temporal resolution as a function of ΣA_i^2. The resolution is fitted as the sum of a jitter and a constant term. The data in the fit belongs to the three 3 pixels read out by FAST2 EVO1 channels.

The difference $x_{trk} - x_{RSD}$ ($y_{trk} - y_{RSD}$) in the $x_{trk} - y_{trk}$ plane is shown for the ST method on the left (right) side of Fig. 16. In these plots, the z scale is limited to two standard deviations (~ 32 µm); with this setting, events above (below) the scale limit are represented with the color of the highest (lowest) bin. As expected, the areas of worse resolution are at the pixel edges and are the source of the non-Gaussian tails present in Fig. 13.

9.2. Effect of electronic noise or amplifier gain miscalibration on the hit position determination

The effect of the electronic noise on the hit position has been studied by adding an uncorrelated Gaussian noise to each of the amplitudes A_i used in the amplitude reconstruction. Fig. 17 (top plot) reports the evolution of the spatial resolution for the dataset taken at 130 V and 190 V as a function of the added RMS noise, while Fig. 17 (bottom plot) shows the same data points against the signal-to-added-noise ratio $A_{pixel}/\sigma_{added\ noise}$. The degradation of the spatial resolution is rather mild as a function of the added noise, and it depends linearly on the noise-to-signal ratio. For values of $A_{pixel}/\sigma_{added\ noise}$ above ~ 50, the measured spatial resolution is reached.

The effects of incorrectly calibrating an amplifier are shown in Fig. 18 for the run taken at bias = 130 V. The result is obtained by calculating the hit position resolution and offset while increasing up to 40% the gain of one of the four amplifiers. The result shows that the position resolution increases by about 20%, and the difference between the mean RSD hit position and the telescope position goes from 0 to 12 µm for a 40% amplifier gain miscalibration.

These two systematic studies demonstrate that the RSD spatial resolution remains very good even if the readout is much noisier than

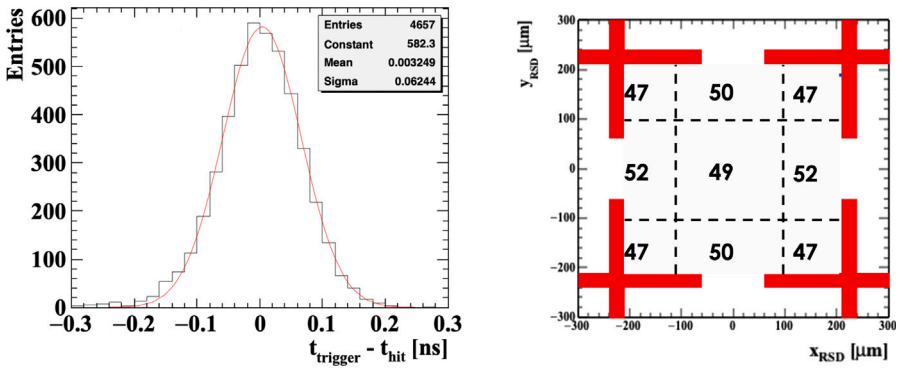

Fig. 20. Left: the distribution $t_{trigger} - t^{hit}$. Right: $\sigma^{hit\ time}$ as a function of the hit position in the pixel. The data shown were collected at bias = 200 V.

FAST2, an important consideration in view of using RSDs in much larger systems.

9.3. Temporal resolution

Given the difficulties in computing the inverse of the covariance matrix, the hit time t^{hit} has been calculated using Eq. (9). The RSD temporal resolution $\sigma^{hit\ time}$ is calculated by subtracting in quadrature from the RMS of the distribution $t_{trigger} - t^{hit}$ the resolution of the trigger, $\sigma_{trigger} = 38 \pm 8$ ps. Since the EVO1 and EVO2 channels of FAST2 have a different signal-to-noise ratio, the results are based only on events collected by the three pixels fully read out by EVO1 channels (see Fig. 4 for details). The results are reported in Fig. 19 as a function of $\sqrt{\Sigma_i^4 A_i^2}$. The resolution is fitted as the sum in quadrature of a constant and a jitter term:

$$\sigma^{hit\ time} = \sqrt{(\sigma^{time-constant})^2 + (\frac{\sigma^{CFD30} \times t^{rise}}{\Sigma_i^4 A_i^2})^2}. \quad (11)$$

The best resolution obtained is $\sigma^{hit\ time} = 49 \pm 6$ ps, dominated by the constant term, $\sigma^{time-constant} = 41 \pm 5$ ps. The constant term is the convolution of contributions coming from the Landau noise, not perfect delay correction, and the FAST2 shape non-linearity.

Fig. 20 (left) shows, for the highest gain point, the distribution of the difference $t_{trigger} - t^{hit}$ while Fig. 20 (right) shows $\sigma^{hit\ time}$ as a function of the hit position in the pixel. The small non-gaussian tails are due to an incorrect delay correction. The temporal resolution is uniform over the pixel surface.

9.4. Using delays to determine the hit position

The signal delays between the hit point and each of the 4 electrodes can be used to calculate the hit position, following a procedure analogous to ST. Two delay types can be used in the position determination: (i) the delays between each electrode and the trigger ($ST^{time\ trigger-el}$) and (ii) between each pair of electrodes ($ST^{time\ el-el}$). For each method, the corresponding templates were calculated using test beam data. Fig. 21 shows the results of these studies and, for comparison, the results of ST: the best resolution obtained with $ST^{time\ trigger-el}$ is about $\sigma \sim 38$ µm, approximately twice that of ST.

10. Conclusions

This paper reports on the determination of the spatial and temporal resolutions of an RSD 450 µm pitch pixels array. The sensor matrix used in this study is part of the second FBK RSD production (RSD2), and it consists of seven 450 µm pitch pixels with cross-shaped electrodes, covering an area of about 1.5 mm^2. The electrodes were read out by the FAST2 ASIC, a 16-channel amplifier fully custom ASIC developed by INFN Torino using 110 nm CMOS technology. The

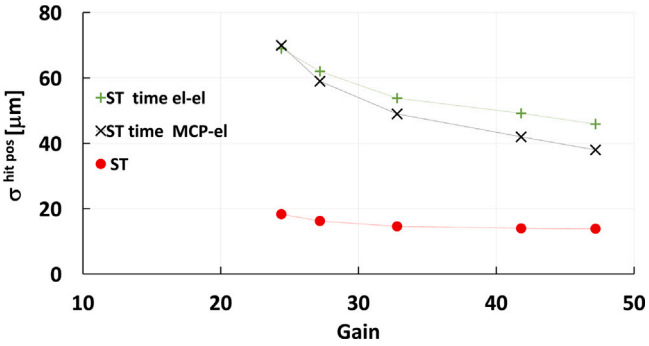

Fig. 21. Spatial resolution as a function of the gain obtained with 3 different methods: ST, $ST^{time\ trigger-el}$, and $ST^{time\ el-el}$.

study was performed at the DESY test beam facility with a 5 GeV/c electron beam. Key findings include achieving a position resolution of $\sigma_x = 14 \pm 1$ µm, approximately 3.5% of the pitch, and a temporal resolution of $\sigma_t = 49 \pm 6$ ps. The study also highlights the 100% fill factor and homogeneous resolutions over the entire matrix surface achieved by RSD sensors. These results confirm the potential of the RSD technology in applications requiring high spatial and temporal resolutions, offering a promising avenue for future developments in particle detection and imaging technologies. Present RSDs are meant for experiments with moderate occupancy; future designs based on DC-coupled RSD will be able to sustain higher occupancy levels.

CRediT authorship contribution statement

L. Menzio: Writing – original draft. **F. Siviero:** Writing – original draft. **R. Arcidiacono:** Writing – review & editing. **N. Cartiglia:** Writing – review & editing, Writing – original draft. **M. Costa:** Writing – review & editing. **T. Croci:** Writing – review & editing. **M. Ferrero:** Writing – review & editing. **C. Hanna:** Writing – review & editing. **L. Lanteri:** Software. **S. Mazza:** Writing – review & editing. **R. Mulargia:** Software. **H-F.W. Sadrozinski:** Writing – review & editing. **A. Seiden:** Writing – original draft. **V. Sola:** Writing – review & editing. **R. White:** Writing – review & editing.

Declaration of competing interest

The authors declare that they have no known competing financial interests or personal relationships that could have appeared to influence the work reported in this paper.

Data availability

Data will be made available on request.

Acknowledgments

The measurements leading to these results have been performed at the test beam facility at DESY Hamburg (Germany), a member of the Helmholtz Association (HGF). This project has received funding from the European Union Horizon Europe research and innovation programme under grant agreement No 101057511. We kindly acknowledge the following funding agencies and collaborations: RD50, Italy, INFN – FBK agreement on sensor production; Dipartimento di Eccellenza, Italy, Univ. of Torino, Italy (ex L. 232/2016, art. 1, cc. 314, 337); Ministero della Ricerca, Italia, PRIN 2017, Italy, Grant 2017L2XKTJ – 4DinSiDe; Ministero della Ricerca, Italia, FARE, Italy, Grant R165xr8frt_fare, Grant TRAPEZIO 2021 Fondazione San Paolo, Torino, Italy.

References

[1] M. Mandurrino, et al., Demonstration of 200-, 100-, and 50- μm pitch resistive AC-coupled silicon detectors (RSD) with 100% fill-factor for 4D particle tracking, IEEE Electr. Device L 40 (11) (2019) 1780, http://dx.doi.org/10.1109/LED.2019.2943242.

[2] N. Cartiglia, et al., 4D tracking: present status and perspectives, Nucl. Inst. Meth. A 1040 (2022) 167228, http://dx.doi.org/10.1016/j.nima.2022.167228, URL https://www.sciencedirect.com/science/article/pii/S0168900222005824.

[3] R. Arcidiacono, et al., High-precision 4D tracking with large pixels using thin resistive silicon detectors, Nucl. Inst. Meth. A 1057 (2023) 168671, http://dx.doi.org/10.1016/j.nima.2023.168671, URL https://www.sciencedirect.com/science/article/pii/S0168900223006617.

[4] M. Tornago, et al., Resistive AC-Coupled Silicon Detectors: principles of operation and first results from a combined analysis of beam test and laser data, Nucl. Inst. Meth. A 1003 (2021) 165319, http://dx.doi.org/10.1016/j.nima.2021.165319, URL https://www.sciencedirect.com/science/article/pii/S016890022100303X. arXiv:2007.09528.

[5] N. Cartiglia, et al., Resistive read-out in thin silicon sensors with internal gain, 2023, arXiv:2301.02968.

[6] R. Diener, et al., The DESY II test beam facility, Nucl. Inst. Meth. A 922 (2019) 265–286, http://dx.doi.org/10.1016/j.nima.2018.11.133.

[7] H. Jansen, et al., Performance of the EUDET-type beam telescopes, EPJ Techn. Instrum. 3 (2016) 7, http://dx.doi.org/10.1140/epjti/s40485-016-0033-2.

[8] J. Baudot, et al., First test results of MIMOSA-26, a fast CMOS sensor with integrated zero suppression and digitized output, in: 2009 IEEE Nuclear Science Symposium Conference Record, NSS/MIC, 2009, pp. 1169–1173, http://dx.doi.org/10.1109/NSSMIC.2009.5402399.

[9] D. Cussans, Description of the JRA1 Trigger Logic Unit (TLU), v0.2c, 2009.

[10] Y. Liu, et al., EUDAQ2—A flexible data acquisition software framework for common test beams, JINST 14 (10) (2019) P10033, http://dx.doi.org/10.1088/1748-0221/14/10/P10033, arXiv:1907.10600.

[11] E. Olave, et al., Design and characterization of the FAST chip: a front-end for 4D tracking systems based on Ultra-Fast Silicon Detectors aiming at 30 ps time resolution, Nucl. Inst. Meth. A 985 (2021) 164615, http://dx.doi.org/10.1016/j.nima.2020.164615, URL https://www.sciencedirect.com/science/article/pii/S0168900220310123.

[12] A.M. Rojas, et al., Amplifier-discriminator ASIC to read out thin Ultra-Fast Silicon Detectors for ps resolution, 2021, pp. 1–4, http://dx.doi.org/10.1109/NSS/MIC44867.2021.9875441.

[13] M. Mandurrino, et al., The second production of RSD at FBK, J. Instrum. 17 (08) (2022) C08001.

[14] Photonis MCP-PMT. URL https://www.photonis.com/products/mcp-pmt.

[15] Teledyne LeCroy HDO940 specifications. URL https://teledynelecroy.com/oscilloscope/waverunner-9000-oscilloscopes/waverunner-9404.

[16] CAEN Logic Unit. URL https://www.caen.it/subfamilies/programmable-logic-unit/.

[17] P. Baesso, D. Cussans, J. Goldstein, The aida-2020 TLU: a flexible trigger logic unit for test beam facilities, AIDA-JINST 14 (09) (2019) P09019, http://dx.doi.org/10.1088/1748-0221/14/09/P09019, arXiv:2005.00310.

[18] CAEN DT5742 16+1 channels digitizer specifications. URL https://www.caen.it/products/dt5742/.

[19] CAEN DT1471LET HV supply specifications. URL https://www.caen.it/products/dt1471et/.

[20] Corrivreckan gitlab project page. URL https://gitlab.cern.ch/corryvreckan/corryvreckan.

[21] S. Siegel, R. Silverman, Y. Shao, S. Cherry, Simple charge division readouts for imaging scintillator arrays using a multi-channel pmt, IEEE Trans. Nucl. Sci. 43 (3) (1996) 1634–1641, http://dx.doi.org/10.1109/23.507162.

[22] A. Apresyan, et al., Measurements of an AC-LGAD strip sensor with a 120 GeV proton beam, J. Instrum. 15 (2020) P09038.

[23] H. Sadrozinski, A. Seiden, N. Cartiglia, 4D tracking with ultra-fast silicon detectors, Rep. Progr. Phys. 81 (2017) 026101, http://dx.doi.org/10.1088/1361-6633/aa94d3.

[24] S. Spannagel, et al., GBL Track Resolution Calculator v2.0, 2016, http://dx.doi.org/10.5281/zenodo.48795.

[25] A.M. Rojas, et al., FAST3: Front-end electronics to read out thin Ultra-Fast Silicon Detectors for ps resolution, 2022, pp. 1–4, http://dx.doi.org/10.1109/LAEDC54796.2022.9908192.

[26] cividec Instrumentation, https://cividec.at.